

Response analysis of NMRG system considering Rb-Xe coupling

Yi Zhang(张燚), Qiyuan Jiang(江奇渊), Bingfeng Sun(孙兵锋), Jiahu Wei(魏加湖), Lin Yang(杨麟), Yongyuan Li(李永远), Zhiguo Wang(汪之国), Kaiyong Yang(杨开勇), and Hui Luo(罗晖)

Citation: Chin. Phys. B, 2024, 33 (**9**): 094203. DOI: 10.1088/1674-1056/ad6130
Journal homepage: http://cpb.iphy.ac.cn; http://iopscience.iop.org/cpb

What follows is a list of articles you may be interested in

Design of a high sensitivity and wide range angular rate sensor based on exceptional surface

Xinsheng Ding(丁鑫圣), Wenyao Liu(刘文耀), Shixian Wang(王师贤), Yu Tao(陶煜), Yanru Zhou(周彦汝), Yu Bai(白禹), Lai Liu(刘来), Enbo Xing(邢恩博), Jun Tang(唐军), and Jun Liu(刘俊)
Chin. Phys. B, 2024, 33 (**8**): 084204. DOI: 10.1088/1674-1056/ad4324

Quasi-anti-parity—time-symmetric single-resonator micro-optical gyroscope with Kerr nonlinearity

Jingtong Geng(耿靖童), Shuyi Xu(徐书逸), Ting Jin(靳婷), Shulin Ding(丁舒林), Liu Yang(杨柳), Ying Wang(王颖), and Yonggang Zhang(张勇刚)
Chin. Phys. B, 2024, 33 (**1**): 014208. DOI: 10.1088/1674-1056/ad0773

Design and simulation of a silicon-based hybrid integrated optical gyroscope system

Dao-Xin Sun(孙道鑫), Dong-Liang Zhang(张东亮), Li-Dan Lu(鹿利单), Tao Xu(徐涛),Xian-Tong Zheng(郑显通), Zhe-Hai Zhou(周哲海), and Lian-Qing Zhu(祝连庆)
Chin. Phys. B, 2023, 32 (**4**): 044212. DOI: 10.1088/1674-1056/ac81a9

Numerical simulation of a truncated cladding negative curvature fiber sensor based on the surface plasmon resonance effect

Zhichao Zhang(张志超), Jinhui Yuan(苑金辉), Shi Qiu(邱石), Guiyao Zhou(周桂耀), Xian Zhou(周娴), Binbin Yan(颜玢玢), Qiang Wu(吴强), Kuiru Wang(王葵如), and Xinzhu Sang(桑新柱)
Chin. Phys. B, 2023, 32 (**3**): 034208. DOI: 10.1088/1674-1056/ac785e

Design of a coated thinly clad chalcogenide long-period fiber grating refractive index sensor based on dual-peak resonance near the phase matching turning point

Qianyu Qi(齐倩玉), Yaowei Li(李耀威), Ting Liu(刘婷), Peiqing Zhang(张培晴),Shixun Dai(戴世勋), and Tiefeng Xu(徐铁峰)
Chin. Phys. B, 2023, 32 (**1**): 014204. DOI: 10.1088/1674-1056/ac6338

Response analysis of NMRG system considering Rb–Xe coupling

Yi Zhang(张燚)[1,2,†], Qiyuan Jiang(江奇渊)[1,2,†], Bingfeng Sun(孙兵锋)[1,2,‡], Jiahu Wei(魏加湖)[3], Lin Yang(杨麟)[3], Yongyuan Li(李永远)[3], Zhiguo Wang(汪之国)[1,2,§], Kaiyong Yang(杨开勇)[1,2], and Hui Luo(罗晖)[1,2]

[1] *College of Advanced Interdisciplinary Studies, National University of Defense Technology, Changsha* 410073, *China*
[2] *Nanhu Laser Laboratory, National University of Defense Technology, Changsha* 410073, *China*
[3] *Huaguan Technology Co., Ltd., Changsha* 410100, *China*

(Received 25 April 2024; revised manuscript received 29 June 2024; accepted manuscript online 10 July 2024)

The dynamic range of the nuclear magnetic resonance gyroscope can be effectively improved through the closed-loop control scheme, which is crucial to its application in inertial measurement. This paper presents the analytical transfer function of Xe closed-loop system in the nuclear magnetic resonance gyroscope considering Rb–Xe coupling effect. It not only considers the dynamic characteristics of the system more comprehensively, but also adds the influence of the practical filters in the gyro signal processing system, which can obtain the accurate response characteristics of signal frequency and amplitude at the same time. The numerical results are compared with an experimentally verified simulation program, which indicate great agreement. The research results of this paper are of great significance to the practical application and development of the nuclear magnetic resonance gyroscope.

Keywords: nuclear magnetic resonance gyroscope, transfer characteristics, Rb–Xe coupling

PACS: 42.81.Pa, 42.79.–e, 74.25.nj, 82.56.–b **DOI:** 10.1088/1674-1056/ad6130

1. Introduction

The nuclear magnetic resonance gyroscope (NMRG) is expected to be one of the most promising quantum gyroscopes with its potential advantages of miniaturization, low power consumption, and acceleration insensitivity, which is quite suitable for future unmanned intelligent small carrier equipment application, and has attracted wide attention in recent years.[1–4] The NMRG achieves rotational measurement by measuring the Larmor precession frequency of nuclear spins with given nuclear species, which is sensitive to the variation of the carrier rotation, and its dynamic range can be effectively improved through the closed-loop control scheme.[5]

However, most of the existing researches focus on the physical principle of NMRG and seek a breakthrough in its performance on this basis,[6–14] while little attention was given to its closed-loop control system and dynamic response characteristics.[5,15] Previous studies only take the closed-loop control characteristics of the Xe spin system into account in the NMRG system, without considering the influence of the embedded Rb magnetometer. Besides, most of the Xe response characteristics research are based on the amplitude steady-state approximation (ASSA),[15,16] which assumes the amplitude of longitudinal and transverse magnetic moment constant in solving spin dynamic equations,[5] while can hardly analyze the dynamic and amplitude response characteristics of NMRG signals. Furthermore, the effects of the phase detection filter in phase-locked loop (PLL) and the low-pass (LP) filter in the built-in Rb magnetometer demodulation procedure are often ignored in these studies, which usually have a significant impact on the actual transfer function of NMRG.

In this paper, the analytical transfer function of Xe closed-loop system in NMRG was obtained by using perturbation theory without applying the ASSA. This transfer function not only considered the dynamic characteristics of the system more comprehensively, but also added the influence of the phase detection filter, which could obtain the response characteristics of signal frequency and amplitude at the same time. In addition, the influence of the PLL filters on the transfer characteristics of NMRG was analyzed and verified with the numerical results of simulation program based on Bloch equation. Then, on this basis, the influence of the embedded Rb magnetometer response characteristics was further considered, and a relatively complete transfer function of NMRG system was constructed and verified. Finally, these theoretical results were applied to the parameter optimization of NMRG system to verify its validity. The research results of this paper are of great significance to the practical application and development of NMRG.

2. Theoretical analysis

Specifically, the signal transfer model of NMRG system to detect carrier rotation information proposed in this paper is shown in Fig. 1.

[†]These authors contributed equally to this work.
[‡]Corresponding author. E-mail: sbf3375038@163.com
[§]Corresponding author. E-mail: maxborn@nudt.edu.cn

© 2024 Chinese Physical Society and IOP Publishing Ltd

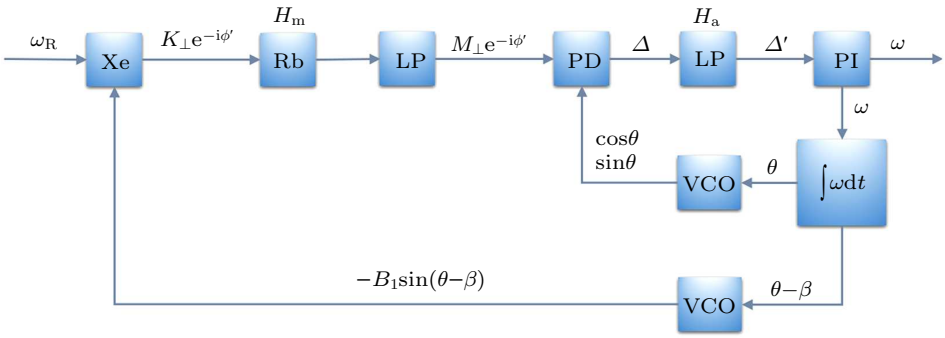


Fig. 1. NMRG rotational signal transfer model.

In Fig. 1 ω_R is the angular rotational velocity of the carrier being measured, which is primarily detected in the NMRG system by the Xe magnetic moment precession signal $K_\perp e^{-i\phi}$. The signal $K_\perp e^{-i\phi}$ is then detected through the Rb magnetic moment precession signal $M_\perp e^{-i\phi'}$, where H_m represented the transfer function of the Rb atomic magnetometer. The resulting $M_\perp e^{-i\phi'}$ signal can be detected by the Faraday rotation effect with photodiode. The bandwidth of the photoelectric conversion and detection system is assumed to be high enough, and the gain of the circuit is absorbed into the signal amplitude $M_\perp$. Similar to the typical PLL, PD is a phase detector, VCO is voltage controlled oscillator, PI represents proportional integral control. For the signal processing and control circuit system, the phase of $M_\perp e^{-i\phi'}$ was first measured as a function of frequency through the PLL, and the phase-tuned signal was then back to the NMRG system via the magnetic field coil in the x direction in order to maintain the stable precession of the Xe magnetic moment, and the precession frequency ω measured by the PLL reflected the carrier rotation. The research work of this study is based on this model.

2.1. Xe magnetic moment closed-loop system response function

For the sake of simplifying analyses, we can first ignore the influence of the embedded Rb atomic magnetometer and only discuss the response function of the Xe magnetic moment closed-loop system. After ignoring the effect of Rb magnetometer and the demodulation LP filter in Fig. 1, the NMRG system dynamics equation can be written as[5]

$$\begin{aligned}
&\dot{K}_z = -\frac{\gamma B_1}{2} K_\perp \cos(\Delta+\beta) + \Gamma_1 (K_0 - K_z),\\
&\dot{K}_\perp = -\Gamma_2 K_\perp + \frac{\gamma B_1}{2} K_z \cos(\Delta+\beta),\\
&\dot{\phi} = \Omega_z - \frac{\gamma B_1}{2}\frac{K_z}{K_\perp}\sin(\Delta+\beta),\\
&\Delta' \approx \mathrm{LP}[\Delta],\\
&\dot{\theta} = g_1\Delta' + g_2\int \Delta' \mathrm{d}t,
\end{aligned} \tag{1}$$

where $\Omega_z = \gamma B_0 + \omega_R$, γ is the gyromagnetic ratio of Xe, B_0 is the static magnetic field strength along z axis, K_0 is the initial Xe magnetic moment, B_1 is the transverse magnetic field strength, g_1 and g_2 are proportion and integral coefficients, Γ_1 and Γ_2 are the longitudinal and transverse relaxation rates of Xe, respectively. ϕ is the precession phase of the Xe magnetic moment, and $K_\perp$, K_z are the transverse and longitudinal components of the Xe magnetic moment, θ is the precession phase of the Xe magnetic moment measured by PLL, β is the phase difference between the Xe transverse precession signal measured by PLL and the set transverse feedback excitation magnetic field $-B_1\sin(\theta-\beta)$.[5] Besides, $\Delta = \phi - \theta$ is the difference between the actual precession phase of the Xe magnetic moment and the phase measured by PLL, which is generally considered to be a small amount. The last two formulas respectively represent the phase-detection LP filter and the PLL loop filter in the closed-loop control. It assumes that the difference between the Xe phase and the phase measured by PLL in the phase detection filter is small, so the influence of trigonometric function can be ignored. In the actual NMRG control system, Butterworth LP filter is usually adopted for simplicity. After specifying the order N and cutoff angular frequency Ω_c, Butterworth LP filter generally has a transfer function

$$H_a(s) = \prod_{k=1}^{N} \frac{1}{\left(\dfrac{s}{\Omega_c} - \exp\left[\dfrac{2k+N-1}{2N}\mathrm{j}\pi\right]\right)}. \tag{2}$$

Equation (1) is a typical nonlinear equation. In order to analyze its response characteristics, it can be considered to expand at the equilibrium position, so as to discuss the dynamic response characteristics of the Xe closed-loop system when the equilibrium position is slightly disturbed. According to Ref. [5], the system has amplitude steady-state solution at equilibrium

$$\begin{aligned}
&\phi - \theta = 0,\\
&\bar{K}_z = \frac{K_0}{1 + \dfrac{(\gamma B_1 \cos\beta)^2}{4\Gamma_1\Gamma_2}},
\end{aligned}$$

$$\bar{K}_\perp = \frac{\gamma B_1}{2}\frac{\cos\beta}{\Gamma_2}\frac{K_0}{1+\frac{(\gamma B_1\cos\beta)^2}{4\Gamma_1\Gamma_2}},$$
$$\bar{\dot{\phi}} = \bar{\omega} = \Omega_z - \Gamma_2\tan\beta, \tag{3}$$

where $\bar{K}_z$, $\bar{K}_\perp$, $\bar{\dot{\phi}}$, and $\bar{\omega}$ denote amplitude steady-state solutions at equilibrium. By expanding Eq. (1) with linear perturbation theory at the equilibrium position shown in Eq. (3), we can obtain

$$\begin{aligned}
\delta\dot{K}_z &\approx -\Gamma_1\cdot\delta K_z - \frac{\gamma B_1}{2}\cos\beta\cdot\delta K_\perp + \frac{\gamma B_1}{2}\bar{K}_\perp\sin\beta\cdot\delta\Delta,\\
\delta\dot{K}_\perp &\approx \frac{\gamma B_1}{2}\cos\beta\cdot\delta K_z - \Gamma_2\cdot\delta K_\perp - \frac{\gamma B_1}{2}\bar{K}_z\sin\beta\cdot\delta\Delta,\\
\delta\dot{\phi} &\approx \delta\Omega_z - \frac{\gamma B_1}{2}\frac{\sin\beta}{\bar{K}_\perp}\cdot\delta K_z + \frac{\gamma B_1}{2}\frac{\bar{K}_z\sin\beta}{\bar{K}_\perp^2}\cdot\delta K_\perp\\
&\quad - \frac{\gamma B_1}{2}\frac{\bar{K}_z}{\bar{K}_\perp}\cos\beta\cdot\delta\Delta,\\
\delta\Delta' &\approx \mathrm{LP}[\delta\Delta],\\
\delta\dot{\theta} &= g_1\delta\Delta' + g_2\int\delta\Delta'\mathrm{d}t.
\end{aligned} \tag{4}$$

By ignoring the tag δ and applying the Laplace transform, we obtain

$$\begin{aligned}
s\tilde{K}_z &\approx -\Gamma_1\cdot\tilde{K}_z - \frac{\gamma B_1}{2}\cos\beta\cdot\tilde{K}_\perp + \frac{\gamma B_1}{2}\bar{K}_\perp\sin\beta\cdot\tilde{\Delta},\\
s\tilde{K}_\perp &\approx \frac{\gamma B_1}{2}\cos\beta\cdot\tilde{K}_z - \Gamma_2\tilde{K}_\perp - \frac{\gamma B_1}{2}\bar{K}_z\sin\beta\cdot\tilde{\Delta},\\
s\tilde{\phi} &\approx \tilde{\Omega}_z - \frac{\gamma B_1}{2}\frac{\sin\beta}{\bar{K}_\perp}\cdot\tilde{K}_z + \frac{\gamma B_1}{2}\frac{\bar{K}_z\sin\beta}{\bar{K}_\perp^2}\cdot\tilde{K}_\perp\\
&\quad - \frac{\gamma B_1}{2}\frac{\bar{K}_z}{\bar{K}_\perp}\cos\beta\cdot\tilde{\Delta},\\
\tilde{\Delta}' &\approx H_\mathrm{a}(s)\cdot\tilde{\Delta},\\
s\tilde{\theta} &= g_1\tilde{\Delta}' + g_2\frac{\tilde{\Delta}'}{s},\\
\tilde{\Delta} &= \tilde{\phi} - \tilde{\theta}.
\end{aligned} \tag{5}$$

The solution can be obtained by

$$\begin{aligned}
\frac{s\tilde{\theta}}{\tilde{\Omega}_z} &= \frac{A+Bs+C_\theta s^2+D_\theta s^3}{A+Es+Fs^2+Gs^3+s^4},\\
\frac{s\tilde{\phi}}{\tilde{\Omega}_z} &= \frac{A+Bs+C_\phi s^2+D_\phi s^3+s^4}{A+Es+Fs^2+Gs^3+s^4},\\
\frac{\tilde{K}_\perp}{\tilde{\Omega}_z} &= \frac{I_\perp s+J_\perp s^2}{K_1(A+Es+Fs^2+Gs^3+s^4)},\\
\frac{\tilde{K}_z}{\tilde{\Omega}_z} &= \frac{I_z s+J_z s^2}{K_1(A+Es+Fs^2+Gs^3+s^4)}.
\end{aligned} \tag{6}$$

Among them

$$\begin{aligned}
A &= g_2H_\mathrm{a}K_1,\\
B &= H_\mathrm{a}(g_2(\Gamma_1+\Gamma_2)+g_1K_1),\\
C_\theta &= H_\mathrm{a}(g_2+g_1(\Gamma_1+\Gamma_2)),\\
D_\theta &= g_1H_\mathrm{a},\\
C_\phi &= (H_\mathrm{a}(g_2+g_1(\Gamma_1+\Gamma_2))+K_1),\\
D_\phi &= (\Gamma_1+\Gamma_2+g_1H_\mathrm{a}),\\
E &= \Gamma_1\Gamma_2^2\sec^2\beta + g_2H_\mathrm{a}(\Gamma_1+\Gamma_2) + g_1H_\mathrm{a}K_1 + \Gamma_2\Omega_\mathrm{d}^2,\\
F &= 2\Gamma_1\Gamma_2 + \Gamma_2^2\sec^2\beta + \Omega_\mathrm{d}^2 + g_2H_\mathrm{a} + g_1H_\mathrm{a}(\Gamma_1+\Gamma_2),\\
G &= (\Gamma_1+2\Gamma_2+g_1H_\mathrm{a}),\\
I_\perp &= -K_0\Gamma_1\Omega_\mathrm{d}(\Gamma_1\Gamma_2 - \Omega_\mathrm{d}^2\cos^2\beta)\sin\beta,\\
J_\perp &= -K_0\Gamma_1\Gamma_2\Omega_\mathrm{d}\sin\beta,\\
I_z &= K_0\Gamma_1\Gamma_2\Omega_\mathrm{d}^2\sin 2\beta,\\
J_z &= \frac{K_0\Gamma_1\Omega_\mathrm{d}^2\sin 2\beta}{2},\\
K_1 &= \Gamma_1\Gamma_2 + \Omega_\mathrm{d}^2\cos^2\beta.
\end{aligned} \tag{7}$$

Here $\Omega_\mathrm{d} = \gamma B_1/2$. The main difference between the results of Eq. (6) and those in Refs. [5,15] is that the ASSA method is adopted in these references to process the transverse and longitudinal signal amplitudes $K_\perp$, K_z in Eq. (1), and the response characteristics $\tilde{K}_\perp/\tilde{\Omega}_z$, $\tilde{K}_z/\tilde{\Omega}_z$ of signal amplitude cannot be obtained. In this paper, the ASSA is not carried out, so the response characteristics of signal amplitude can be obtained.

From Eq. (6) and considering the relation $\Omega_z = \gamma B_0 + \omega_\mathrm{R}$, the rotational response function and the fluctuation response function of the main magnetic field of the Xe closed-loop system can be obtained

$$\begin{aligned}
\frac{s\tilde{\theta}}{\tilde{\omega}_\mathrm{R}} &= \frac{A+Bs+C_\theta s^2+D_\theta s^3}{A+Es+Fs^2+Gs^3+s^4},\\
\frac{s\tilde{\theta}}{\tilde{B}_0} &= \gamma\frac{A+Bs+C_\theta s^2+D_\theta s^3}{A+Es+Fs^2+Gs^3+s^4}.
\end{aligned} \tag{8}$$

2.2. Rb atomic magnetometer transfer function

The embedded Rb atomic magnetometer in NMRG satisfies Bloch equation[17]

$$\begin{aligned}
\left(\frac{\mathrm{d}}{\mathrm{d}t} + \frac{1}{\tau_2} + \mathrm{i}\gamma_\mathrm{Rb}B_z\right)M_+ &= \mathrm{i}\gamma_\mathrm{Rb}M_zB_+,\\
\frac{\mathrm{d}}{\mathrm{d}t}M_z &= \mathrm{Re}\left[\mathrm{i}\gamma_\mathrm{Rb}B_+^*M_+\right] + \frac{M_0-M_z}{\tau_1},
\end{aligned} \tag{9}$$

where $M_+ = M_x + \mathrm{i}M_y$ and M_z are Rb transverse and longitudinal magnetic moments, respectively, M_0 is the initial Rb magnetic moment, $B_+ = B_x + \mathrm{i}B_y = B_\perp\mathrm{e}^{-\mathrm{i}\omega_1 t}$ represents the external transverse magnetic field to be measured, B_+^* means its complex conjugation, and $B_z = B_0 + B_\mathrm{c}\cos\omega_\mathrm{c}t$ is the z-direction magnetic field, B_c and ω_c are the carrier field strength and frequency, respectively. γ_Rb is the gyromagnetic ratio of Rb, τ_2 is the Rb transverse relaxation time. Using the series expansion method, we can obtain[17]

$$\begin{aligned}
M_x^{np} &= -\tau_2\gamma^\mathrm{Rb}B_1M_0\sin(p\omega_\mathrm{c}t)C_{pn-}[\cos\phi - D_{n-}\sin\phi]\\
&\quad + \tau_2\gamma^\mathrm{Rb}B_1M_0\cos(p\omega_\mathrm{c}t)C_{pn-}[\sin\phi + D_{n-}\cos\phi],\\
M_y^{np} &= \tau_2\gamma^\mathrm{Rb}B_1M_0\sin(p\omega_\mathrm{c}t)C_{pn-}[\sin\phi + D_{n-}\cos\phi]
\end{aligned}$$

$$+\tau_2\gamma^{\mathrm{Rb}}B_1M_0\cos\left(p\omega_{\mathrm{c}}t\right)C_{pn-}\left[\cos\phi-D_{n-}\sin\phi\right], \quad (10)$$

where $\phi=\omega_{\mathrm{l}}t$, and

$$\begin{aligned} D_{n\pm} &= \tau_2\left(\gamma^{\mathrm{Rb}}B_0+n\omega_{\mathrm{c}}\pm\omega_{\mathrm{l}}\right), \\ C_{pn\pm} &= \frac{\mathrm{J}_n\left(\dfrac{\gamma^{\mathrm{Rb}}B_{\mathrm{c}}}{\omega_{\mathrm{c}}}\right)\mathrm{J}_{n-p}\left(\dfrac{\gamma^{\mathrm{Rb}}B_{\mathrm{c}}}{\omega_{\mathrm{c}}}\right)}{1+D_{n\pm}^2}, \end{aligned} \quad (11)$$

where $\mathrm{J}_n(\cdot)$ denotes the n-th order first-type Bessel function. The embedded Rb magnetometer usually utilizes $\cos\left(p\omega_{\mathrm{c}}t-\alpha\right)$ to demodulate the X-direction magnetic moment signal, and considering the positive and negative frequency combinations, we can obtain

$$\begin{aligned} \mathrm{sig} &= \mathrm{LP}\left\{M_x^{np>0}\cdot\cos\left(p\omega_{\mathrm{c}}t-\alpha\right)\right\} \\ &= \frac{\tau_2\gamma^{\mathrm{Rb}}M_0B_1}{2}\left(A_2\sin\phi+B_2\cos\phi\right) \\ &= \frac{\tau_2\gamma^{\mathrm{Rb}}M_0B_1}{2}\sqrt{A_2^2+B_2^2}\sin\left(\phi+\arctan\frac{B_2}{A_2}\right). \end{aligned} \quad (12)$$

Among them

$$\begin{aligned} A_2 &= \sum_{n=-\infty}^{+\infty}\left(C_{pn-}+C_{-pn-}\right)\cos\alpha \\ &\quad +\left(C_{pn-}-C_{-pn-}\right)D_{n-}\sin\alpha, \\ B_2 &= \sum_{n=-\infty}^{+\infty}\left(C_{pn-}+C_{-pn-}\right)D_{n-}\cos\alpha \\ &\quad -\left(C_{pn-}-C_{-pn-}\right)\sin\alpha. \end{aligned} \quad (13)$$

Therefore, according to the definition, considering the influence of Eq. (12) on signal amplitude and phase, and adding the influence of LP filter $H_{\mathrm{LP}}(\mathrm{j}\omega_{\mathrm{l}})$ during demodulation, the transfer function of Rb magnetometer in NMRG system can be written as follows:

$$\begin{aligned} \frac{\tilde{M}_x^p}{\tilde{B}_+} &= H_{\mathrm{m}}(\mathrm{j}\omega_{\mathrm{l}}) \\ &= \frac{\tau_2\gamma^{\mathrm{Rb}}M_0}{2}\left[A_2(\omega_{\mathrm{l}})+\mathrm{j}B_2(\omega_{\mathrm{l}})\right]H_{\mathrm{LP}}(j\omega_{\mathrm{l}}). \end{aligned} \quad (14)$$

If further taken $p=1$, $n=1$, $H_{\mathrm{m}}(\mathrm{j}\omega_{\mathrm{l}})$ can be simplified as

$$\begin{aligned} H_{\mathrm{m}}(\mathrm{j}\omega_{\mathrm{l}}) &\approx \frac{\tau_2\gamma^{\mathrm{Rb}}M_0}{2}\left(1+\mathrm{j}D_-\right) \\ &\quad\times\left(C_1\,\mathrm{e}^{-\mathrm{j}\alpha}+C_{-1}\,\mathrm{e}^{\mathrm{j}\alpha}\right)H_{\mathrm{LP}}(\mathrm{j}\omega_{\mathrm{l}}). \end{aligned} \quad (15)$$

Among them

$$\begin{aligned} D_- &= \tau_2\left(\gamma^{\mathrm{Rb}}B_0+\omega_{\mathrm{c}}-\omega_{\mathrm{l}}\right), \\ C_1 &= \frac{\mathrm{J}_1\left(\dfrac{\gamma^{\mathrm{Rb}}B_{\mathrm{c}}}{\omega_{\mathrm{c}}}\right)\mathrm{J}_0\left(\dfrac{\gamma^{\mathrm{Rb}}B_{\mathrm{c}}}{\omega_{\mathrm{c}}}\right)}{1+D_-^2}, \\ C_{-1} &= \frac{\mathrm{J}_1\left(\dfrac{\gamma^{\mathrm{Rb}}B_{\mathrm{c}}}{\omega_{\mathrm{c}}}\right)\mathrm{J}_2\left(\dfrac{\gamma^{\mathrm{Rb}}B_{\mathrm{c}}}{\omega_{\mathrm{c}}}\right)}{1+D_-^2}. \end{aligned} \quad (16)$$

2.3. Transfer function of NMRG closed-loop system

Generally, the NMRG system carries out closed-loop control by detecting the precession phase of the transverse magnetic moment of Xe, thus we mainly focus on the effect of the Rb magnetometer on the transverse magnetic moment phase of Xe. According to the Rb magnetometer transfer function, the phase effect is

$$\phi'=\phi+\angle H_{\mathrm{m}}(\mathrm{j}\omega_{\mathrm{l}}). \quad (17)$$

For the response to rotation ω_{R}, since Rb has a relatively large gyromagnetic ratio, it can be assumed that the magnetometer frequency is mainly determined by the magnetic field and the influence from rotation can be ignored. The precession frequency $\dot{\phi}$ of Xe magnetic moment in the above equation can be expanded by perturbation at its equilibrium position $\bar{\omega}_{\mathrm{l}}$ to obtain

$$\phi'\approx\phi+\angle H_{\mathrm{m}}(\mathrm{j}\bar{\omega}_{\mathrm{l}})+\left.\frac{\partial\angle H_{\mathrm{m}}}{\partial\omega_{\mathrm{l}}}\right|_{\bar{\omega}_{\mathrm{l}}}\left(\dot{\phi}-\bar{\omega}_{\mathrm{l}}\right). \quad (18)$$

As for the response to the fluctuation of the main magnetic field B_0, both Rb and Xe are significantly affected, so equation (17) can be expanded as follows:

$$\begin{aligned} \phi' &\approx \phi+\angle H_{\mathrm{m}}(\mathrm{j}\bar{\omega}_{\mathrm{l}})+\left.\frac{\partial\angle H_{\mathrm{m}}}{\partial\omega_{\mathrm{l}}}\right|_{\bar{\omega}_{\mathrm{l}}}\left(\dot{\phi}-\bar{\omega}_{\mathrm{l}}\right) \\ &\quad+\left.\frac{\partial\angle H_{\mathrm{m}}}{\partial B_0}\right|_{\bar{B}_0}\left(B_0-\bar{B}_0\right). \end{aligned} \quad (19)$$

Therefore, by substituting the above phase effect of magnetometer into Eq. (4), the rotational response perturbation equation of NMRG system signal after considering the influence of Xe closed-loop system and Rb magnetometer simultaneously can be obtained. For details, as shown in Eq. (20)

$$\begin{aligned} \delta\dot{K}_z &\approx -\Gamma_1\cdot\delta K_z-\frac{\gamma B_1}{2}\cos\beta'\cdot\delta K_\perp \\ &\quad+\frac{\gamma B_1}{2}\bar{K}_\perp\sin\beta'\cdot\left[\delta\Delta-\partial_{\omega_{\mathrm{l}}}\angle H_{\mathrm{m}}\delta\dot{\phi}\right], \\ \delta\dot{K}_\perp &\approx \frac{\gamma B_1}{2}\cos\beta'\cdot\delta K_z-\Gamma_2\cdot\delta K_\perp \\ &\quad-\frac{\gamma B_1}{2}\bar{K}_z\sin\beta'\cdot\left[\delta\Delta-\partial_{\omega_{\mathrm{l}}}\angle H_{\mathrm{m}}\delta\dot{\phi}\right], \\ \delta\dot{\phi} &\approx \delta\Omega_z-\frac{\gamma B_1}{2}\frac{\sin\beta'}{\bar{K}_\perp}\cdot\delta K_z+\frac{\gamma B_1}{2}\frac{\bar{K}_z\sin\beta'}{\bar{K}_\perp^2}\cdot\delta K_\perp \\ &\quad-\frac{\gamma B_1}{2}\frac{\bar{K}_z}{\bar{K}_\perp}\cos\beta'\cdot\left[\delta\Delta-\partial_{\omega_{\mathrm{l}}}\angle H_{\mathrm{m}}\delta\dot{\phi}\right], \\ \delta\dot{\phi}' &\approx \delta\dot{\phi}+\partial_{\omega_{\mathrm{l}}}\angle H_{\mathrm{m}}\delta\ddot{\phi}, \\ \delta\Delta &= \delta\phi'-\delta\theta, \\ \delta\Delta' &\approx \mathrm{LP}\left[\delta\Delta\right], \\ \delta\dot{\theta} &= g_1\delta\Delta'+g_2\int\delta\Delta'\,\mathrm{d}t. \end{aligned} \quad (20)$$

Here, it is redefined $\Delta = \phi' - \theta$ according to the signal transfer mode in Fig. 1, and the phase difference between the magnetic moment precept of the Xe closed-loop system and the transverse feedback magnetic field becomes $\phi - \theta + \beta = \phi' - \angle H_{\rm m} - \theta + \beta = \Delta - \angle H_{\rm m} + \beta$, which can be abbreviated as $\Delta - \partial_{\omega_{\rm l}} \angle H_{\rm m} \left(\dot{\phi} - \bar{\omega}_{\rm l}\right) + \beta - \angle \bar{H}_{\rm m}$, after substituting into the approximate formula of Eq. (18), where the last two terms are constants $\beta' = \beta - \bar{H}_{\rm m}$. Then replace Δ and β in Eq. (4) by the first and last two terms of $\Delta - \partial_{\omega_{\rm l}} \angle H_{\rm m} \left(\dot{\phi} - \bar{\omega}_{\rm l}\right) + \beta - \angle \bar{H}_{\rm m}$ respectively, equation (20) can be obtained. Similar to Eq. (5), after the Laplace transform and ignoring the tag δ, we can get

$$
\begin{aligned}
s\tilde{K}_z &\approx -\Gamma_1 \cdot \tilde{K}_z - \frac{\gamma B_1}{2} \cos\beta' \cdot \tilde{K}_\perp \\
&\quad + \frac{\gamma B_1}{2} \bar{K}_\perp \sin\beta' \cdot \left[\tilde{\Delta} - \partial_{\omega_{\rm l}} \angle H_{\rm m} s\tilde{\phi}\right], \\
s\tilde{K}_\perp &\approx \frac{\gamma B_1}{2} \cos\beta' \cdot \tilde{K}_z - \Gamma_2 \tilde{K}_\perp \\
&\quad - \frac{\gamma B_1}{2} \bar{K}_z \sin\beta' \cdot \left[\tilde{\Delta} - \partial_{\omega_{\rm l}} \angle H_{\rm m} s\tilde{\phi}\right], \\
s\tilde{\phi} &\approx \tilde{\Omega}_z - \frac{\gamma B_1}{2} \frac{\sin\beta'}{\bar{K}_\perp} \cdot \tilde{K}_z + \frac{\gamma B_1}{2} \frac{\bar{K}_z \sin\beta'}{\bar{K}_\perp^2} \cdot \tilde{K}_\perp \\
&\quad - \frac{\gamma B_1}{2} \frac{\bar{K}_z}{\bar{K}_\perp} \cos\beta \cdot \left[\tilde{\Delta} - \partial_{\omega_{\rm l}} \angle H_{\rm m} s\tilde{\phi}\right], \\
s\tilde{\phi}' &\approx s\tilde{\phi} + \partial_{\omega_{\rm l}} \angle H_{\rm m} s^2 \tilde{\phi}, \\
\tilde{\Delta} &= \tilde{\phi}' - \tilde{\theta}, \\
\tilde{\Delta}' &\approx H_{\rm a}(s) \cdot \tilde{\Delta}, \\
s\tilde{\theta} &= g_1 \tilde{\Delta}' + g_2 \frac{\tilde{\Delta}'}{s}.
\end{aligned} \tag{21}
$$

The rotational response function of the NMRG system required in this paper can be obtained by solving Eq. (21) of the multivariate linear equations $s\tilde{\theta}/\tilde{\omega}_{\rm R}$

$$
\begin{aligned}
\frac{s\tilde{\theta}}{\tilde{\omega}_{\rm R}} &= \frac{A_3 + B_3 s + C_3 s^2 + D_3 s^3 + E_3 s^4}{F_3 + G_3 s + H_3 s^2 + I_3 s^3 + s^4}, \\
A_3 &= H_{\rm a} g_2 \left(\Gamma_1\Gamma_2 + \Omega_{\rm d}^2 \cos^2\beta'\right), \\
B_3 &= H_{\rm a}\left[g_2\left(\Gamma_1 + \Gamma_2\right) + \left(g_1 + g_2 \partial_{\omega_{\rm l}} \angle H_{\rm m}\right)\right. \\
&\quad \left. \times \left(\Gamma_1\Gamma_2 + \Omega_{\rm d}^2 \cos^2\beta'\right)\right], \\
C_3 &= H_{\rm a}\left[g_2 + \left(\Gamma_1 + \Gamma_2\right)\left(g_1 + g_2 \partial_{\omega_{\rm l}} \angle H_{\rm m}\right)\right. \\
&\quad \left. + g_1 \partial_{\omega_{\rm l}} \angle H_{\rm m} \left(\Gamma_1\Gamma_2 + \Omega_{\rm d}^2 \cos^2\beta'\right)\right], \\
D_3 &= H_{\rm a}\left[g_1 + g_2 \partial_{\omega_{\rm l}} \angle H_{\rm m} + g_1\left(\Gamma_1 + \Gamma_2\right) \partial_{\omega_{\rm l}} \angle H_{\rm m}\right], \\
E_3 &= H_{\rm a} g_1 \partial_{\omega_{\rm l}} \angle H_{\rm m}, \\
F_3 &= H_{\rm a} g_2 \left(2\Gamma_2 \partial_{\omega_{\rm l}} \angle H_{\rm m} + \cos^2\beta'\right) \\
&\quad \times \left(\Gamma_1\Gamma_2 + \Omega_{\rm d}^2 \cos^2\beta'\right) \sec^2\beta', \\
G_3 &= \left(H_{\rm a}\left(g_1\Gamma_1\Gamma_2 + g_2\left(\Gamma_1 + \Gamma_2 - \Gamma_1\Gamma_2 \partial_{\omega_{\rm l}} \angle H_{\rm m}\right)\right)\right. \\
&\quad + \Omega_{\rm d}^2\left(\Gamma_2 + g_1 H_{\rm a} \cos^2\beta'\right. \\
&\quad \left. \left. - H_{\rm a} g_2 \partial_{\omega_{\rm l}} \angle H_{\rm m} \sin^2\beta' + g_1\Gamma_2 H_{\rm a} \partial_{\omega_{\rm l}} \angle H_{\rm m}\right)\right. \\
&\quad \left. - \Gamma_2^2\left(\left(g_2 + 2g_1\Gamma_2\right) H_{\rm a} \partial_{\omega_{\rm l}} \angle H_{\rm m} - \Gamma_1\right) \sec^2\beta'\right), \\
H_3 &= \left(g_2 H_{\rm a} + g_1\Gamma_1 H_{\rm a} + \Gamma_2 H_{\rm a}\left(g_1 - g_2 \partial_{\omega_{\rm l}} \angle H_{\rm m}\right)\right. \\
&\quad + \Gamma_1\Gamma_2\left(2 - g_1 H_{\rm a} \partial_{\omega_{\rm l}} \angle H_{\rm m}\right) + \Omega_{\rm d}^2 \\
&\quad - \Omega_{\rm d}^2 H_{\rm a} g_1 \partial_{\omega_{\rm l}} \angle H_{\rm m} \sin^2\beta' \\
&\quad \left. + \Gamma_2^2\left(1 - H_{\rm a} g_1 \partial_{\omega_{\rm l}} \angle H_{\rm m}\right) \sec^2\beta'\right), \\
I_3 &= \Gamma_1 + g_1 H_{\rm a} + \Gamma_2\left(2 - g_1 H_{\rm a} \partial_{\omega_{\rm l}} \angle H_{\rm m}\right).
\end{aligned} \tag{22}
$$

Similarly, for the fluctuation of the main magnetic field, equation (19) can be used to replace Δ, β in Eq. (4) to obtain the perturbation equation of the fluctuation response of the main magnetic field B_0 of the NMRG system signal considering the influence of the Xe closed-loop system and the Rb magnetometer

$$
\begin{aligned}
\delta\dot{K}_z &\approx -\Gamma_1 \cdot \delta K_z - \frac{\gamma B_1}{2} \cos\beta' \cdot \delta K_\perp \\
&\quad + \frac{\gamma B_1}{2} \bar{K}_\perp \sin\beta' \cdot \left[\delta\Delta - \partial_{\omega_{\rm l}} \angle H_{\rm m} \delta\dot{\phi} - \partial_{B_0} \angle H_{\rm m} \delta B_0\right], \\
\delta\dot{K}_\perp &\approx \frac{\gamma B_1}{2} \cos\beta' \cdot \delta K_z - \Gamma_2 \cdot \delta K_\perp \\
&\quad - \frac{\gamma B_1}{2} \bar{K}_z \sin\beta' \cdot \left[\delta\Delta - \partial_{\omega_{\rm l}} \angle H_{\rm m} \delta\dot{\phi} - \partial_{B_0} \angle H_{\rm m} \delta B_0\right], \\
\delta\dot{\phi} &\approx \gamma \delta B_0 - \frac{\gamma B_1}{2} \frac{\sin\beta'}{\bar{K}_\perp} \cdot \delta K_z + \frac{\gamma B_1}{2} \frac{\bar{K}_z \sin\beta'}{\bar{K}_\perp^2} \cdot \delta K_\perp \\
&\quad - \frac{\gamma B_1}{2} \frac{\bar{K}_z}{\bar{K}_\perp} \cos\beta' \cdot \left[\delta\Delta - \partial_{\omega_{\rm l}} \angle H_{\rm m} \delta\dot{\phi} - \partial_{B_0} \angle H_{\rm m} \delta B_0\right], \\
\delta\dot{\phi}' &\approx \delta\dot{\phi} + \partial_{\omega_{\rm l}} \angle H_{\rm m} \delta\ddot{\phi} + \partial_{B_0} \angle H_{\rm m} \delta\dot{B}_0, \\
\delta\Delta &= \delta\phi' - \delta\theta, \\
\delta\Delta' &\approx LP[\delta\Delta], \\
\delta\dot{\theta} &= g_1 \delta\Delta' + g_2 \int \delta\Delta' {\rm d}t.
\end{aligned} \tag{23}
$$

According to the method of Eq. (4), the fluctuation response characteristics $s\tilde{\theta}/\tilde{B}_0$ of the main magnetic field of the NMRG system considering Rb–Xe coupling can be obtained by using Eq. (23)

$$
\begin{aligned}
\frac{s\tilde{\theta}}{\tilde{B}_0} &= \frac{A_4 + B_4 s + C_4 s^2 + D_4 s^3 + E_4 s^4}{F_4 + G_4 s + H_4 s^2 + I_4 s^3 + s^4}, \\
A_4 &= g_2 H_{\rm a}\left(\Gamma_2 \partial_{B_0} \angle H_{\rm m} + \gamma_{\rm Xe} \cos^2\beta'\right) \\
&\quad \times \left(\Gamma_1\Gamma_2 + \Omega_{\rm d}^2 \cos^2\beta'\right) \sec^2\beta', \\
B_4 &= H_{\rm a}\left(\left[g_2\Gamma_2\gamma_{\rm Xe} + g_1\Gamma_1\Gamma_2\gamma_{\rm Xe}\right.\right. \\
&\quad \left. + g_2\Gamma_1\left(\gamma_{\rm Xe} + 2\Gamma_2 \partial_{B_0} \angle H_{\rm m} + \Gamma_2\gamma_{\rm Xe} \partial_{\omega_{\rm l}} \angle H_{\rm m}\right)\right] \\
&\quad + \Omega_{\rm d}^2\left(g_2 \partial_{B_0} \angle H_{\rm m} + g_1\Gamma_2 \partial_{B_0} \angle H_{\rm m}\right. \\
&\quad + g_1\gamma_{\rm Xe} \cos^2\beta' + g_2\gamma_{\rm Xe} \partial_{\omega_{\rm l}} \angle H_{\rm m} \cos^2\beta') \\
&\quad \left. + \left(g_2 + g_1\Gamma_1\right)\Gamma_2^2 \partial_{B_0} \angle H_{\rm m} \sec^2\beta'\right), \\
C_4 &= H_{\rm a}\left(g_2\left[\gamma_{\rm Xe} + \left(\Gamma_1 + 2\Gamma_2\right) \partial_{B_0} \angle H_{\rm m}\right.\right. \\
&\quad \left. + \left(\Gamma_1 + \Gamma_2\right)\gamma_{\rm Xe} \partial_{\omega_{\rm l}} \angle H_{\rm m}\right] \\
&\quad + g_1\left[\Gamma_2\gamma_{\rm Xe} + \Gamma_1\left(\gamma_{\rm Xe} + 2\Gamma_2 \partial_{B_0} \angle H_{\rm m} + \Gamma_2\gamma_{\rm Xe} \partial_{\omega_{\rm l}} \angle H_{\rm m}\right)\right] \\
&\quad + \Omega_{\rm d}^2 g_1 \partial_{B_0} \angle H_{\rm m} + \Omega_{\rm d}^2 g_1 \gamma_{\rm Xe} \partial_{\omega_{\rm l}} \angle H_{\rm m} \cos^2\beta' \\
&\quad \left. + g_1\Gamma_2^2 \partial_{B_0} \angle H_{\rm m} \sec^2\beta'\right), \\
D_4 &= H_{\rm a}\left(g_2\left(\partial_{B_0} \angle H_{\rm m} + \gamma_{\rm Xe} \partial_{\omega_{\rm l}} \angle H_{\rm m}\right)\right.
\end{aligned}
$$

$$
\begin{aligned}
&+g_1\left[\gamma_{\mathrm{Xe}}+\left(\Gamma_1+2\Gamma_2\right)\partial_{B_0}\angle H_{\mathrm{m}}\right.\\
&\left.+\left(\Gamma_1+\Gamma_2\right)\gamma_{\mathrm{Xe}}\partial_{\omega_{\mathrm{l}}}\angle H_{\mathrm{m}}\right]\Big),\\
E_4 &= g_1 H_{\mathrm{a}}\left(\partial_{B_0}\angle H_{\mathrm{m}}+\gamma_{\mathrm{Xe}}\partial_{\omega_{\mathrm{l}}}\angle H_{\mathrm{m}}\right),\\
F_4 &= g_2 H_{\mathrm{a}}\left(\cos^2\beta'-\Gamma_2\partial_{\omega_{\mathrm{l}}}\angle H_{\mathrm{m}}\right)\\
&\cdot\left(\Gamma_1\Gamma_2+\Omega_{\mathrm{d}}^2\cos^2\beta'\right)\sec^2\beta',\\
G_4 &= \Big(H_{\mathrm{a}}\left[g_1\Gamma_1\Gamma_2+g_2\left(\Gamma_1+\Gamma_2-\Gamma_1\Gamma_2\partial_{\omega_{\mathrm{l}}}\angle H_{\mathrm{m}}\right)\right]\\
&-\Gamma_2^2\left[-\Gamma_1+\left(g_2+g_1\Gamma_1\right)H_{\mathrm{a}}\partial_{\omega_{\mathrm{l}}}\angle H_{\mathrm{m}}\right]\sec^2\beta'\\
&+\Omega_{\mathrm{d}}^2\Big(\Gamma_2-g_1\Gamma_2 H_{\mathrm{a}}\partial_{\omega_{\mathrm{l}}}\angle H_{\mathrm{m}}+g_1 H_{\mathrm{a}}\cos^2\beta'\\
&-g_2 H_{\mathrm{a}}\partial_{\omega_{\mathrm{l}}}\angle H_{\mathrm{m}}\sin^2\beta'\Big)\Big),\\
H_4 &= \Big(g_1\Gamma_1 H_{\mathrm{a}}+\Gamma_1\Gamma_2\left(2-g_1 H_{\mathrm{a}}\partial_{\omega_{\mathrm{l}}}\angle H_{\mathrm{m}}\right),\\
&+\Omega_{\mathrm{d}}^2\left(1-g_1 H_{\mathrm{a}}\partial_{\omega_{\mathrm{l}}}\angle H_{\mathrm{m}}\right)\\
&+H_{\mathrm{a}}\left(g_2+g_1\Gamma_2-g_2\Gamma_2\partial_{\omega_{\mathrm{l}}}\angle H_{\mathrm{m}}\right)\\
&-\Gamma_2^2\left(g_1 H_{\mathrm{a}}\partial_{\omega_{\mathrm{l}}}\angle H_{\mathrm{m}}-1\right)\sec^2\beta'\Big),\\
I_4 &= \Gamma_1+g_1 H_{\mathrm{a}}+\Gamma_2\left(2-g_1 H_{\mathrm{a}}\partial_{\omega_{\mathrm{l}}}\angle H_{\mathrm{m}}\right).
\end{aligned}
\tag{24}
$$

The fluctuation response function of the main magnetic field given in Eq. (24) is helpful to study the influence of Z-direction magnetic field changes on the signals of the NMRG system, and can improve the magnetic compensation performance of the NMRG system through parameter optimizations.

3. Simulation analysis and verification

To verify the effectiveness of the established theoretical model and further make analysis accordingly, a published and verified simulation program of NMRG is utilized here to make comparison.[6,18] In fact, the simulation system uses almost the same data processing and feedback control procedures as the real experimental system, on the other hand, the gyro signal in the simulation system is obtained by solving Bloch equation which has been verified by a lot of literatures,[2,5,19] which ensures the credibility of the simulation results. Figure 2 gives an example of how accurate the utilized simulation program of NMRG could be, where the maximum relative error between the experimental and simulation results is only 6.26×10^{-5}.

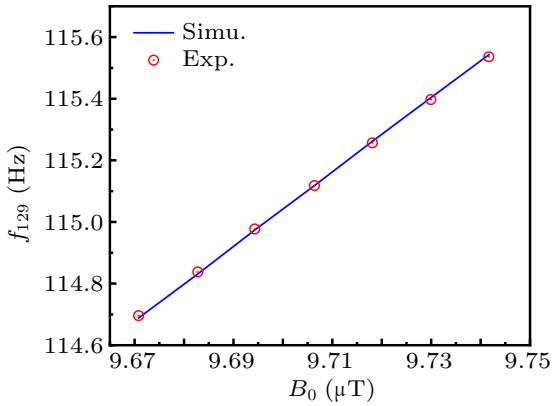


Fig. 2. Comparisons of precession frequency change between NMRG simulation (Simu.) system and experimental (Exp.) system.

Another reason why the simulation system is preferred here to verify the established theoretical model in this paper is that compared with a real system, all system parameters such as the polarization and relaxation time of the simulation system are known accurately, which is more conducive to guarantee the accuracy of the verification.

3.1. Xe magnetic moment closed-loop system response characteristics

Firstly, the response characteristics of the Xe magnetic moment closed-loop system without considering the effect of Rb magnetometer are verified by the established NMRG signal simulation program. This part of the simulation also omits the Bloch equation for Rb atomic system. In addition to phase detection filter and PLL loop filter, other physical parameters of the NMRG simulation program are shown in Table 1.

Table 1. Xe closed-loop system simulation and theoretical calculation of physical parameters.

Γ_1 (s^{-1})	Γ_2 (s^{-1})	γ (rad/μT)	B_1 (nT)	β (rad)
1/20	1/10	$-2\pi\times11.86$	1.8	0

To check the accuracy of Eq. (8), figures 3 and 4 show the theoretical and simulation results of the NMRG amplitude–frequency and phase–frequency response curves under the conditions of different phase detection filters and PLL loop filters.

The abscissa in Figs. 3 and 4 is the fluctuation frequency of the carrier rotation signal, and the circles denote the simulation results, the solid lines are the results of the theoretical formula. In the phase–frequency curves, in order to make the curves continuous, translations were made for phases exceeding 360°.

It can be seen that the amplitude–frequency response curve and the phase–frequency response curve are both in good agreement with the simulation results, which can verify the correctness of the theoretical formula. Alternatively, one can also find that the amplitude–frequency and phase–frequency curves are both significantly correlated with the parameters of the phase detection filter and the PLL loop filter. Furthermore, by comparing Figs. 3 and 4, it can be seen that the PLL loop filter parameters have larger impact on the amplitude–frequency response curve, while the phase detection filter parameters have larger impact on the phase–frequency response curve. Thus, in order to predict accurate response characteristics in the analysis of NMRG systems, one must consider not only the physical system itself based on the Bloch equation, but should also take into account the influence of various filters in the signal transfer process.

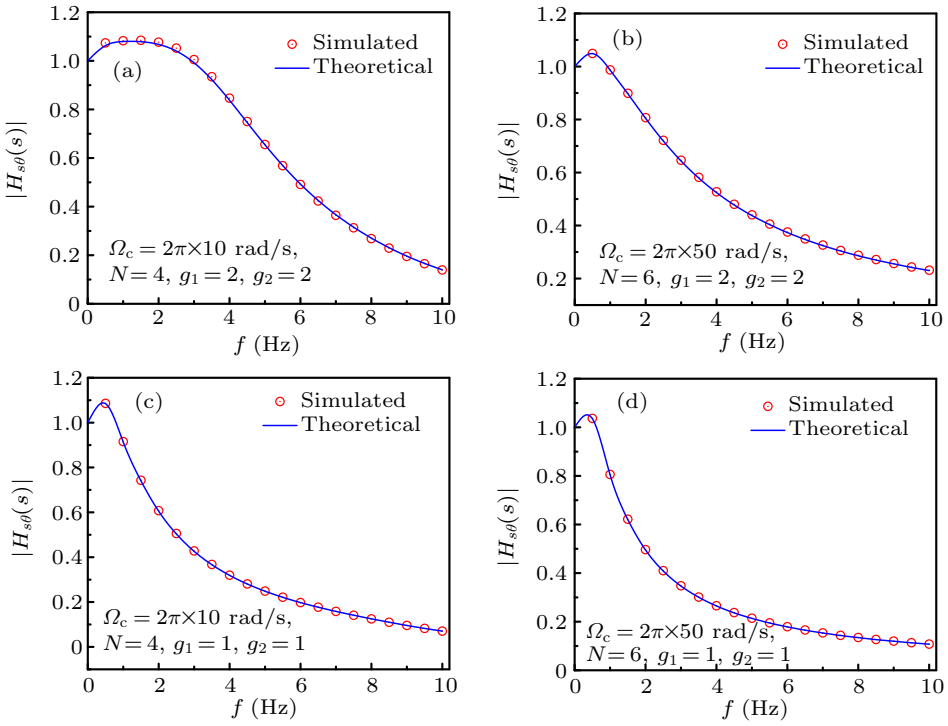


Fig. 3. Theoretical and simulation results of NMRG amplitude–frequency response curve under different phase filter and loop filter conditions.

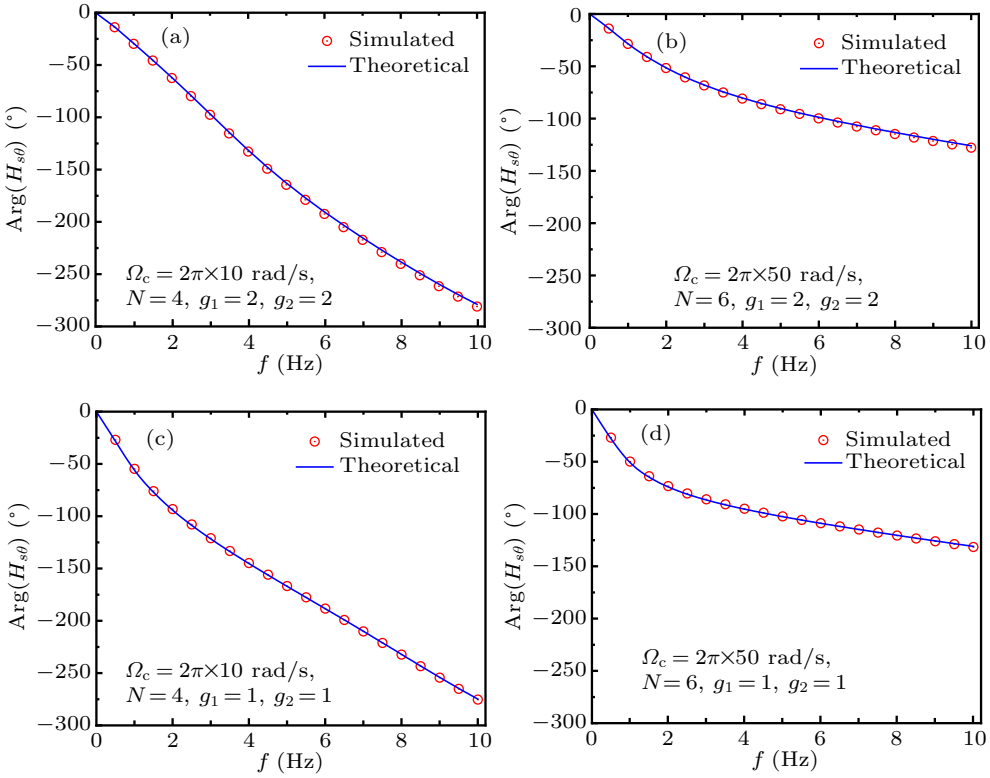


Fig. 4. The theory and simulation results of NMRG phase–frequency response curve under different phase filter and loop filter conditions.

In order to further analyze the impact of these parameters on the system response, figures 5 and 6 show the amplitude–frequency and phase–frequency response curves of parameters Ω_c, N, g_1, g_2 separately changed with other parameters remain unchanged. The set values of the unchanged parameters are $\Omega_c = 2\pi \times 10$ rad/s, $N = 4$, $g_1 = 2$, $g_2 = 2$. From Fig. 5(a), it can be observed that increasing the bandwidth of the phase detector filter alone leads to a slight decrease in the amplitude–frequency response curve within 8 Hz and a slight increase outside 8 Hz. However, observing the system phase–frequency curve in Fig. 6(a), it can be observed that the system phase delay significantly decreases with the increase of the bandwidth of the phase detector filter, which is consistent with general experience. Unlike this, as shown in Fig. 5(b),

increasing the order of the phase detector filter significantly affects the amplitude frequency response characteristics of the system, and the peak response of the system increases significantly with the increase of the filter order. Meanwhile, the phase delay of the system in Fig. 6(b) will also increase with the increase of filter order N. Finally, figures 5(c), 5(d) and 6(c), 6(d) show that the proportional control parameter g_1 of the loop filter has a significant impact on the amplitude frequency and phase frequency response characteristics of the system, while the integral control parameter g_2 has a relatively small impact on the system characteristics. Furthermore, from Figs. 5 and 6, it can be observed that adjusting one of these filter parameters alone cannot effectively improve the system response bandwidth. In order to effectively optimize the system response characteristics, a multi parameter collaborative adjustment method may be needed. We will discuss this issue in Section 4.

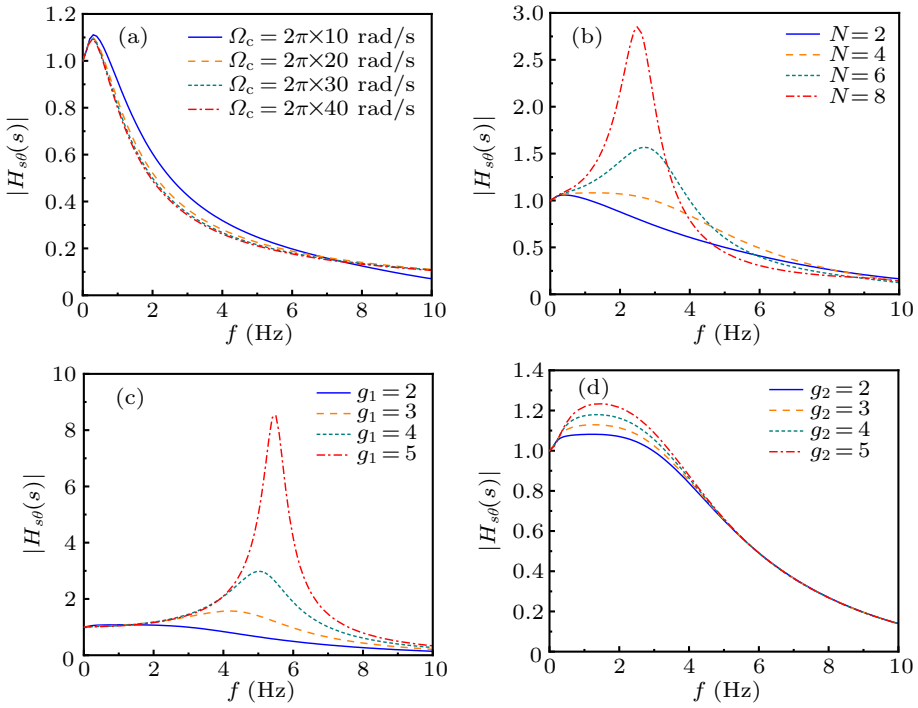


Fig. 5. Theoretical amplitude–frequency response curves with different phase detector filter and loop filter parameters.

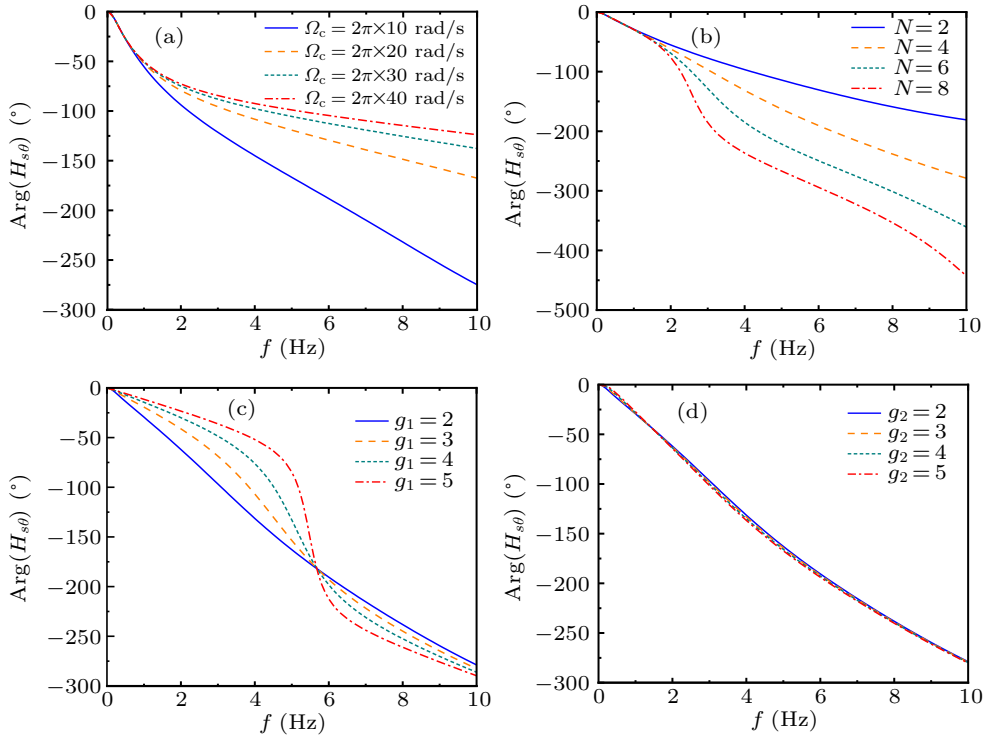


Fig. 6. Theoretical phase–frequency response curves with different phase detector filter and loop filter parameters.

By further observation of Eq. (6), it contains not only the response characteristics of frequency signal $s\tilde{\theta}/\tilde{\omega}_{\rm R}$, but also the response characteristics of transverse amplitude signal $\tilde{K}_{\perp}/\tilde{\omega}_{\rm R}$. Therefore, the comparison of the amplitude response characteristics for the transverse amplitude can be obtained by the theoretical formula and the simulation system, as shown in Fig. 7(a). It can be seen that the transverse amplitude signal has a typical LP characteristic to the fluctuation frequency of the rotating signal, and the accurate consistency between the theoretical and simulation results further verifies the correctness of the theoretical formula.

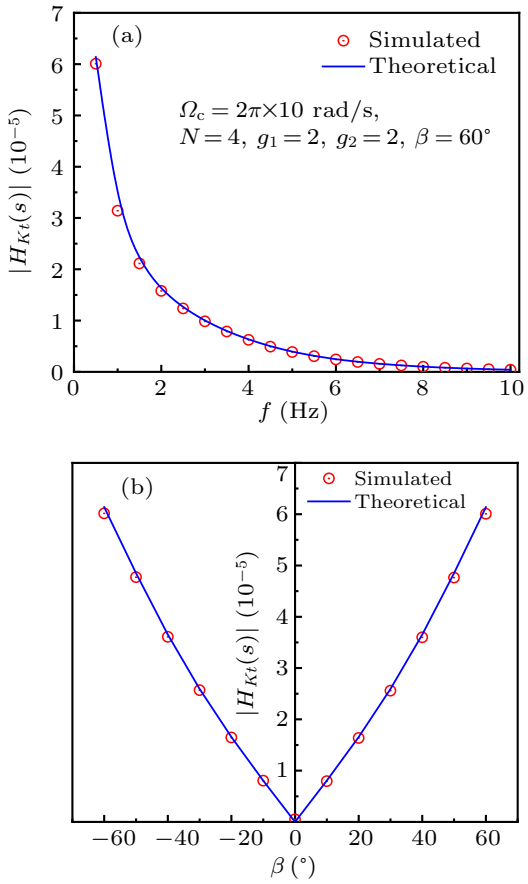


Fig. 7. (a) Comparisons of theoretical and simulation results of rotational response of NMRG lateral amplitude signal; (b) 0.5-Hz response characteristics of transverse amplitude signals with different closed-loop phases.

It also shows that factors $I_{\perp}$ and $J_{\perp}$ in Eq. (6) both contain a factor $\sin\beta$. Thus, when the closed-loop phase β is zero, the response of the transverse amplitude signal becomes zero, which can be used as an important criterion for adjusting the closed-loop phase parameter β of the actual NMRG system. Figure 7(b) shows the response of the transverse amplitude of 0.5 Hz at different closed-loop phases β, where the consistency between the theoretical and simulation results verifies the above conclusion.

In order to further analyze the difference between Eq. (6) and ASSA results, figure 8 shows the amplitude response characteristics obtained under the same conditions. A comparison in Fig. 8(a) shows that as the bandwidth of the phase detector filter increases, the influence of the phase detector filter gradually decreases, and the amplitude–frequency response characteristics of Eq. (6) gradually approach the ASSA results which not considering the phase detector filter. This not only verifies the correctness of Eq. (6), but also shows that in the actual system, when the bandwidth of the phase detector filter is small, its influence on the system response characteristics cannot be ignored. On the other hand, figure 8(b) shows the change of amplitude response of the ASSA and Eq. (6) with the closed-loop phase β when the angular velocity fluctuates at the frequency of 0.5 Hz. It can be seen that the results agree well when β is small, but there is a significant difference when β is greater than 60°. However, in the actual NMRG experiment, the closed-loop phase β is usually not so large, and the ASSA results still have great applicability.

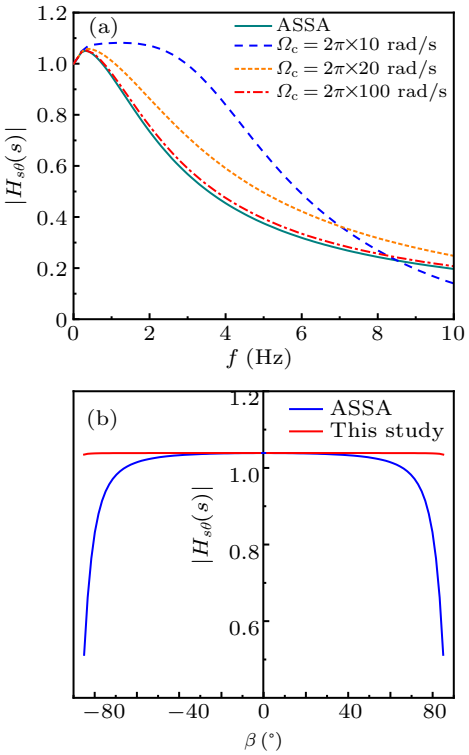


Fig. 8. (a) Amplitude–frequency response curves of ASSA and different phase detector filter bandwidths, (b) 0.5-Hz response characteristics of ASSA and Eq. (6) with different closed-loop phase β.

3.2. Verification of Rb atomic magnetometer transfer characteristics

In order to construct a complete signal transfer model of NMRG system, the transfer function formula of the embedded Rb magnetometer in NMRG is given in Subsection 2.2 through theoretical analysis. In order to verify the correctness of the theoretical formula, the amplitude and phase response characteristics of Rb atomic magnetometer to the transverse magnetic field frequency with different carrier demodulation LP filters are compared in Fig. 9, respectively. Table 2 shows the relevant physical parameters set in the theoretical calculation and the simulation. Note that the magnetic moment has

been converted into the corresponding magnetic field here for the convenience of calculation, so the magnetic field unit is μT as given in Table 2.

Table 2. Physical parameters of Rb atomic magnetometer system simulation and theoretical calculation.

τ_2 (s)	$\gamma_{\rm Rb}$ (rad/μT)	M_0 (μT)	$\omega_{\rm c}$ (rad)	$B_{\rm c}$ (μT)	α (rad)
0.0001	$-2\pi\times 6998.0$	0.005	$2\pi\times 69980$	13.57	0

As can be seen in Fig. 9, the amplitude–frequency curve obtained by Eq. (15) (solid line) is in good agreement with the results given by the simulation program (circles) under the same physical parameter conditions. The small errors (maximum relative error about 2%) in the amplitude–frequency curves in Figs. 9(a) and 9(b) come mainly from the cut-off error in Eq. (15), where only the $n=1$ term is considered. When taking the sum of the terms $n=-10$ to $n=10$ in Eq. (13), the numerical calculation results show that this maximum relative error will decrease from 2% to 0.8%. Secondly, figure 9 shows that the parameters of the demodulation LP filter can significantly affect its amplitude and phase frequency response characteristics, so the influence of the filter parameters should be carefully considered in performance analysis and optimization of actual NMRG system. In addition, a close look at Figs. 9(c) and 9(d) reveals that the phase delay of the input signal of embedded Rb magnetometer varies with different frequencies, so there may be significant phase differences in the magnetic moment precession signals of ^{129}Xe and ^{131}Xe measured simultaneously in NMRG. This has a negative impact on the dynamic characteristics of the final output signal of the gyroscope synthesized from these dual isotope precession signals and the magnetic field compensation signal. This phase delay may need to be considered for correction and compensation during the actual development of NMRG.

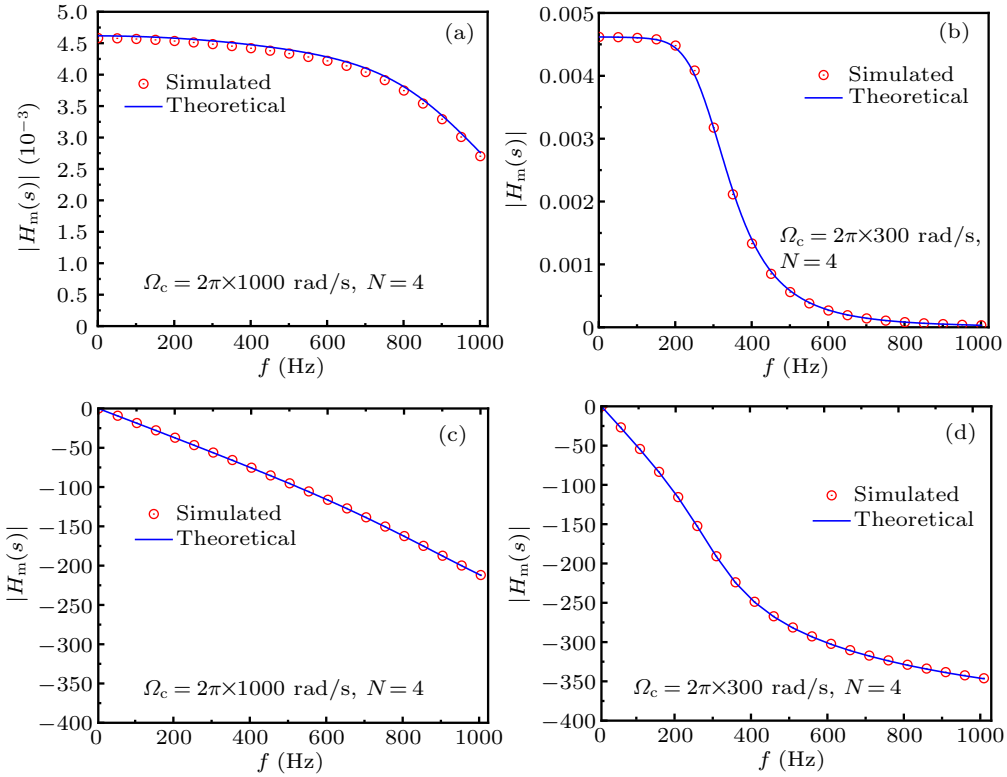


Fig. 9. (a), (b) Rb atomic magnetometer with different carrier demodulation low pass filter amplitude response to the rotation frequency of a transverse magnetic field, (c), (d) Rb atomic magnetometer with different carrier demodulation low pass filter characteristics of phase response to transverse magnetic field rotation frequency.

3.3. Verification of NMRG closed-loop system response characteristics

After verifying the correctness of the response characteristics of the Xe magnetic moment closed-loop system and the embedded Rb atomic magnetometer, the simulation program is also used to verify the rotational and main magnetic field fluctuation response characteristics of the complete NMRG system given in Eqs. (22) and (24). The parameters applied in simulation here were still the same as listed in Tables 1 and 2.

Figure 10 shows the rotational response characteristics of the Rb–Xe coupled NMRG system under different filter parameters. The circle is from the simulation results, and the solid line is from the theoretical Eq. (22). N' and $\Omega_{\rm c}'$ denote the order and cutoff angular frequency of the LP filter in demodulation procedure related to $H_{\rm LP}(\mathrm{j}\omega_{\rm l})$ in Eq. (15). It can be seen that the theoretical results are in good agreement with the simulation ones, which can verify the correctness of the Rb–Xe coupled NMRG rotational response model. In addition, it can be seen from Fig. 10 that PI parameters have a sig-

nificant impact on the rotational response characteristics of the NMRG system. Finally, by comparing Fig. 10 with Figs. 3 and 4, it can be found that since the Rb magnetometer has a large bandwidth for relatively small rotations, and Rb atoms are relatively insensitive to rotation, it has little impact on the system response characteristics, resulting in the similar response characteristics of the same parameters in Fig. 10 and in Figs. 3 and 4.

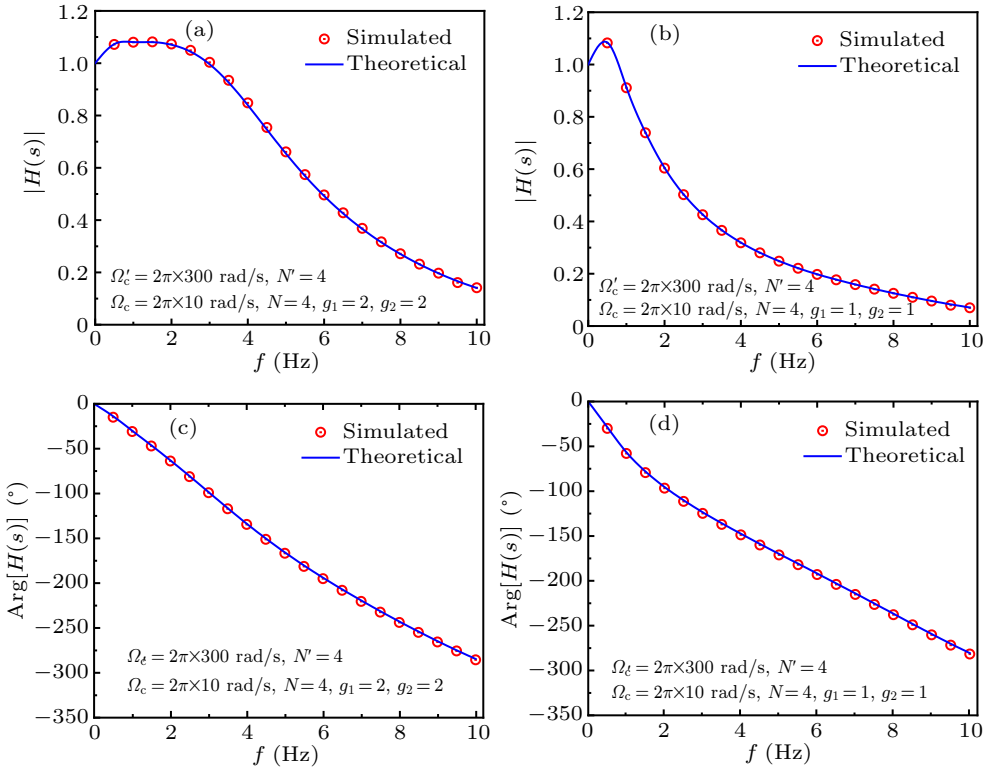


Fig. 10. (a), (b) Rotational amplitude–frequency and (c), (d) rotational phase–frequency response characteristics of NMRG systems considering different loop filter parameters after Rb–Xe coupling.

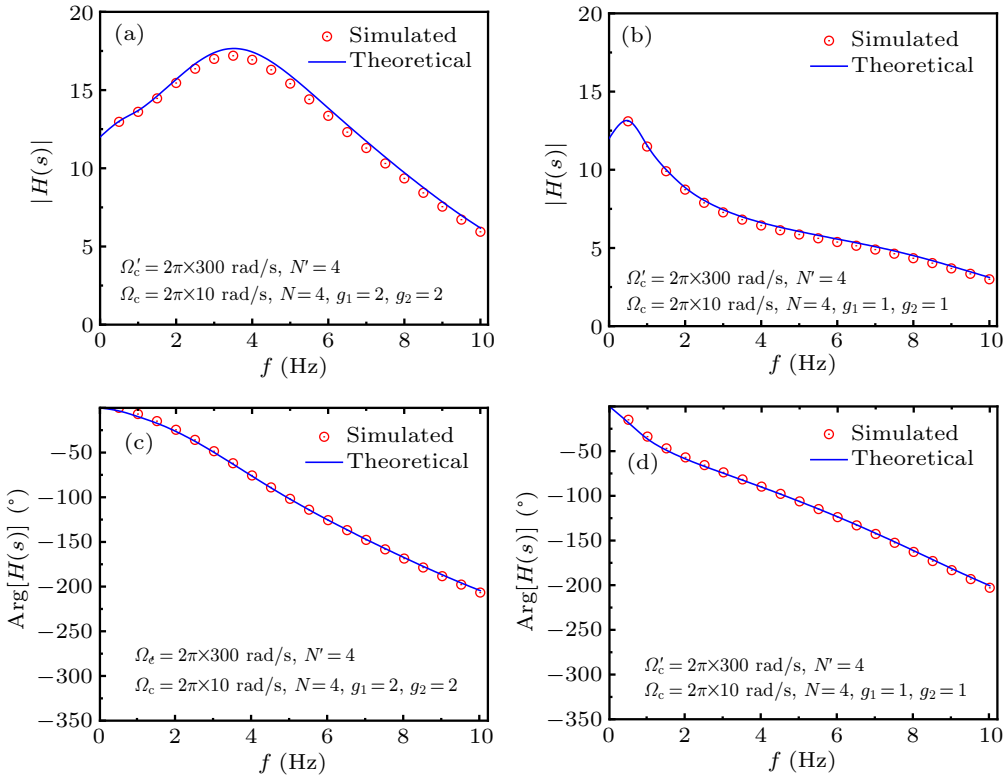


Fig. 11. (a), (b) Considering different loop filter parameters after Rb–Xe coupling amplitude–frequency response of the main magnetic field fluctuation in NMRG system, (c), (d) considering different loop filter parameters after Rb–Xe coupling phase–frequency response characteristics of main magnetic field fluctuation in NMRG system.

The fluctuation response characteristics of the main magnetic field B_0 of the Rb–Xe coupled NMRG system under different parameter settings are shown in Fig. 11. The circles are from simulation results, and the solid lines are from Eq. (22). Note that the errors between the theoretical and simulation results are primarily due to the approximate treatment schemes, such as the truncation of Eq. (15), ignoring the influence of magnetometer on signal amplitude when dealing with Rb–Xe coupling in Eq. (17), and neglecting the influence of the transverse feedback magnetic field when analyzing the response characteristics of the magnetometer. By comparison of Fig. 10 along with Fig. 11, the rotational response characteristics of the NMRG system can be found to be significantly different from the response characteristics of the fluctuations of the main magnetic field, which is primarily due to the influence of the main magnetic field on the transfer characteristics of the Rb magnetometer as can be seen from Eq. (19). This needs special attention in NMRG when achieving dynamic compensation of the main magnetic field through Xe nuclear magnetic moment precession frequency.

4. Parameter optimization application

In general, along with the development of the NMRG system, the atomic polarization intensity, relaxation time, and other physical parameters will have relatively well-defined values, which are not easily controlled by external conditions. While signal processing systems such as the phase-detection LP filter and the PLL loop filter are easy to control and tune. Thus, as an application of the theoretical formula derived above, we primarily investigated the influence rule of the phase-detection filter and the PLL loop filter on the amplitude–frequency response characteristics of the rotational signal of the NMRG system. The calculated results of the theoretical formula are shown in Fig. 12. With the exception of the phase detection filter and the PLL loop filter, the settings in Tables 1 and 2 are still adopted. The parameters $\Omega_c = 2\pi \times 10$ rad/s, $N = 4$, $g_1 = 2$, $g_2 = 2$ are adopted if both filters are unspecified.

Figure 12(a) shows the variation of the NMRG rotational amplitude–frequency response curve as a function of the phase detector filter bandwidth. As can be seen, increasing the phase detector filter bandwidth only slightly increases the amplitude of the high-frequency response of the system, but instead decreases the amplitude of the low-frequency response, which cannot effectively increase the rotational response bandwidth of the NMRG system.

The variation of the NMRG rotation amplitude response curve as a function of the PLL loop filter parameter g_1 is shown in Fig. 12(b). It can be seen that increasing the filter parameter g_1 alone can effectively increase the rotation response, particularly if the rotation signal frequency is above 5 Hz. However, one can also notice that the amplitude of the response is much greater than 1 in the part where the frequency variation of the rotation signal is greater than 5 Hz. In other words, this will severely distort the dynamic scaling factor of the NMRG system, as well as reducing the stability of the PLL itself, which is easy to cause unlocking phenomena.

Likewise, figure 12(c) shows the variation of the NMRG rotational amplitude–frequency response curve with the PLL loop filter parameter g_2. It can be seen that increasing filter parameter g_2 only increases the low-frequency response of the system. These three figures indicate that changing the parameters of the phase detection filter and the PLL loop filter alone cannot effectively improve the response bandwidth of the NMRG system.

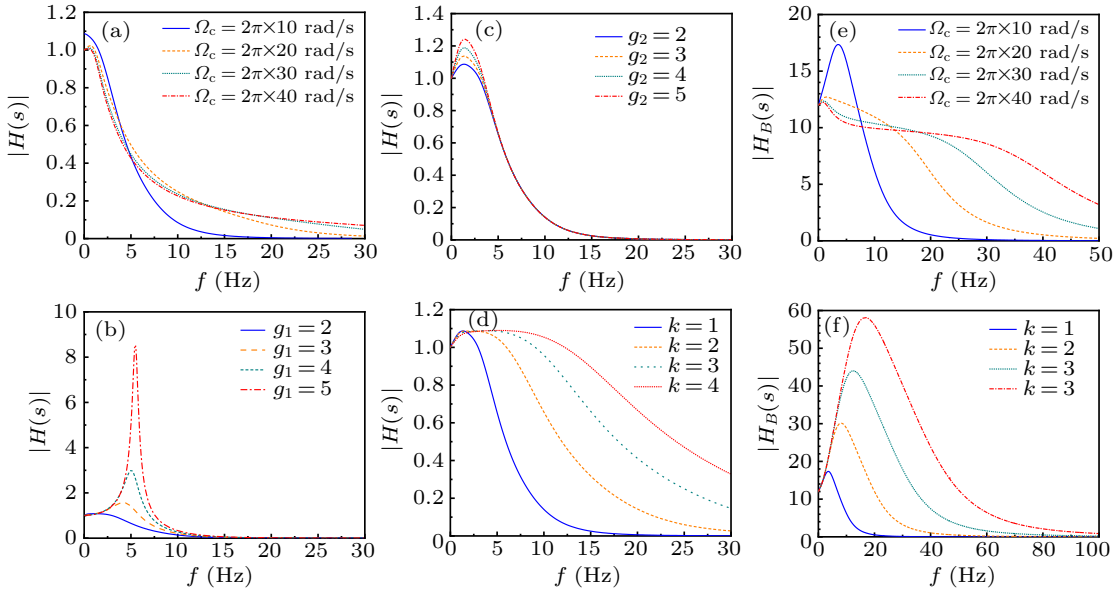


Fig. 12. The influence of the phase-discriminating LP filter and the PLL loop filter parameters on amplitude–frequency response characteristics of rotational signals in NMRG system.

However, in Fig. 12(d), it shows that the rotational response bandwidth of the NMRG system can be effectively improved by tuning the filter parameters Ω_c, g_1, g_2 in a specific proportion. The specific parameters corresponding to the curves in the figure are $(\Omega_c = k\cdot 2\pi\times 10, g_1 = k\cdot 2, g_2 = k^2\cdot 2)$. This method can be explained by classical PLL theory.[20] Usually, there are two typical filtering parameters of a second order PLL, undamped natural frequency ω_n and dimensionless damping coefficient ξ, which can be used to represent the bandwidth and dynamic response capability of the loop, respectively. The relationship between them and filtering parameters g_1, g_2 defined in this paper is as follows, where K_d and K_V are the gain coefficients of the phase detector and VCO in the loop, respectively

$$\omega_n = \sqrt{K_d K_V g_2}, \tag{25}$$

$$\xi = \frac{g_1}{2}\sqrt{\frac{K_d K_V}{g_2}}. \tag{26}$$

Therefore, the method in this paper extends the bandwidth of the loop while keeping the dynamic loop response parameters ξ unchanged. It can be seen from Fig. 12 that the response bandwidth of the NMRG systems increases significantly as the proportional coefficient k is increased, while still maintaining a response range that is essentially the same. At $k = 4$, the bandwidth of the response is fundamentally 10 Hz, which is important when optimizing the performance of real NMRG systems.

Similarly, figures 12(e) and 12(f) show the influence rule of the parameters of the phase detector filter and the PLL loop filter on the amplitude–frequency response characteristics of the NMRG system's main magnetic field fluctuations. It can be seen that the influence of loop filter parameters g_1, g_2 on the amplitude–frequency response characteristics of the main magnetic field fluctuation is similar to that on the rotational response characteristics, but the influence of the phase detection filter bandwidth is more significant. It can be seen from Figs. 12(e) and 12(f) that the response bandwidth of the main magnetic field fluctuation of the NMRG system is mainly affected by the phase detection filter bandwidth.

5. Conclusion

In this paper, the analytical transfer function of Xe closed-loop system considering Rb–Xe coupling effect in NMRG is obtained by using perturbation theory without the ASSA. The theoretical results are compared with a verified simulation program based on Bloch equation, and the well matched results prove the correctness of the theoretical formula. Meanwhile, through theoretical calculations and simulations, it can be found that filter parameters have a significant impact on the system response characteristics. Thus, in order to predict accurate response characteristics in the analysis of NMRG systems, one must consider not only the physical system itself based on the Bloch equation, but should also take into account the influence of various filters in the signal transfer process. In addition, the influence of filter parameters on the system response bandwidth was studied using the proposed theoretical formulas in this paper, and an effective method for setting filter parameters to improve the NMRG rotational response bandwidth was proposed. These theoretical formulas and analytical results are of great significance to the practical application and development of NMRG.

Acknowledgements

Project supported by the Natural Science Foundation of China (Grant Nos. 61701515 and U23B2066), the Natural Science Foundation of Hunan Province, China (Grant No. 2021JJ40700), and the Research Project of National University of Defense Technology (Grant No. ZK22-18).

References

[1] Meyer D and Larsen M 2014 *Gyroscopy and Navigation* **5** 75
[2] Kornack T W, Ghosh R K and Romalis M V 2005 *Phys. Rev. Lett.* **95** 230801
[3] Fang J and Qin J 2012 *Sensors* **12** 6331
[4] Kitching J, Knappe S and Donley E A 2011 *IEEE Sens. J.* **11** 1749
[5] Walker T G and Larsen M S 2016 *Adv. Atom. Mol. Opt. Phys.* **65** 373
[6] Zhang Y, Wang Z, Jiang Q, *et al.* 2020 *Navigation and Control* **19** 18
[7] Vershovskii A K, Litmanovich Y A, Pazgalev A S, *et al.* 2018 *Gyroscopy and Navigation* **9** 162
[8] Bulatowicz M, Griffith R, Larsen M, *et al.* 2013 *Phys. Rev. Lett.* **111** 102001
[9] Jia Y, Liu Z, Zhou B, *et al.* 2019 *J. Phys. D: Appl. Phys.* **52** 355001
[10] Jiang Q, Luo H, Yang K, *et al.* 2019 *Navigation Positioning & Timing* **6** 92
[11] Sheng D, Kabcenell A and Romalis M 2014 *Phys. Rev. Lett.* **113** 163002
[12] Zhan X, Chen C, Wang Z, *et al.* 2020 *AIP Adv.* **10** 045002
[13] Wang Z, Li J and Xiong Z 2020 *OSA Continuum.* **3** 903
[14] Acosta R H, Agulles L, Komin S, *et al.* 2006 *Phys. Chem. Chem. Phys.* **8** 4182
[15] Jiang Q, Wang Z, Zhan X, *et al.* 2019 *AIP Adv.* **9** 125220
[16] Zhang K, Zhao N and Wang Y 2020 *Sci. Rep-UK.* **10** 2258
[17] Jiang Q, Li J, Wang Z, *et al.* 2019 *AIP Adv.* **9** 045117
[18] Chen C, Zhang Y, Wang Z, *et al.* 2021 *Chin. Phys. B* **30** 050707
[19] Zhang Y, Li J, Jiang Q, *et al.* 2022 *J. Magn. Reson.* **344** 107295
[20] Garder F M 2017 *Phaselock Techniquse*, 3rd Edn. (Posts and Telecommunications Press) pp. 10, 11